






Wavelength selective beam-steering in a dual-mode multi-layer plasmonic laser

MAHIN AHAMED,^{1,†}  MD. NASIM AFROJ,^{1,†}
SHADMAN SHAHID,^{1,2,†} 
AND MUHAMMAD ANISUZZAMAN TALUKDER^{1,*} 

¹Department of Electrical and Electronic Engineering, Bangladesh University of Engineering and Technology, Bangladesh

²Department of Computer Science and Engineering, BRAC University, Bangladesh

[†]These co-authors are equal contributors.

*anis@ee.buet.ac.bd

Abstract: Due to its improved localization and confinement of light in single or multiple wavelength modes, nanolasers based on plasmonic crystals have grown in popularity in recent years. However, the lasing modes are not spatially separated, making applying different modes to different applications difficult. This work demonstrates an effective technique for spatially separating the two modes of a merged lattice metal nanohole array-based dual-mode plasmonic laser. A flat dielectric metasurface-based beam-splitter that exploits phase gradient profiles on the interfaces has been added to the laser to separate the modes into distinct spatial beams. The proposed structure successfully separates two modes by $\sim 23^\circ$, and the separation can be raised to $\sim 63^\circ$ by tuning structural parameters such as the radius of the nanocylinders and the number of supercell rows. In addition, multiple beams can be generated, allowing for manual beam steering. This approach has a high emission output with a narrow linewidth, clarity, and a substantial degree of future tunability potential. The proposed integrated structure will provide a novel means of device miniaturization and may also serve advanced optical applications such as optical communication, quantum optics, interferometry, spectroscopy, and light detection and ranging (LiDAR).

© 2024 Optica Publishing Group under the terms of the [Optica Open Access Publishing Agreement](#)

1. Introduction

Beam steering is a technique for modifying the direction of the main lobe of radiation emitted from an electromagnetic source. It has found applications in acoustic and optical systems [1]. Traditional optical beam steering methods manipulate refractive index or use external mechanical components like mirrors, prisms, lenses, or transmission diffraction gratings [2–6]. Although these techniques have been adapted for steering the output beam of semiconductor lasers [7–9], they often compromise on system speed, size, and lifespan, thereby necessitating the search for more efficient alternatives.

In recent decades, nanophotonics concepts have driven efforts in miniaturizing optical devices down to nanoscale dimensions. Plasmonics—one of the key fields of nanophotonics—has made it possible to confine light at sub-wavelength dimensional devices. Plasmonic lasers stand out as significant nanophotonic coherent light sources. Their operation and physics primarily depend on the excitation of specific plasmonic modes, namely surface plasmon polariton (SPP) and localized surface plasmon (LSP) [10]. These miniaturized lasers have diverse applications, including biomedical sensing, bio-molecule detection, imaging, spectroscopy, efficient on-chip optical interconnects, nanolithography, and the integration of optical and microelectronic devices [11–18].

The concept of stimulated emission in plasmonic structures was initially theorized in 2003 [19]. However, it was not until 2007 that experimental evidence was reported in the near-infrared spectrum using metallic components [20]. Since then, research in plasmonic nanolasers (PNLs) has advanced significantly, enhancing design effectiveness, lowering thresholds, and enabling strong directed emission in visible and near-infrared wavelength regimes through various topologies [21–24]. PNLs capable of generating coherent beams in multiple wavelengths provide an expansive array of applications beyond their more commonly studied single-mode counterparts. Such multi-mode coherent sources are particularly relevant where space and fabrication constraints exist.

Consequently, plasmonic multi-mode lasers have recently captured increased research interest. Pourjamal et al. achieved dual-mode lasing by disrupting the symmetry of a two-dimensional (2D) ferromagnetic nickel plasmonic nanodisk array [25]. A viscous quantum-dot film paired with a plasmonic nanoparticle lattice was utilized by Winkler et al. to demonstrate dual-wavelength lasing [26]. Shahid et al. recently proposed planar multi-layer PNL designs for dual-mode lasing in the near-infrared range [27,28], one with a metal nanohole array (NHA) and the other with a distributed Bragg reflector (DBR) integrated into the lasing cavity. However, their application is limited since the multiple lasing modes are not spatially separated. Simultaneous access to both wavelength modes can be achieved by creating adequate spatial separation between them via separate beam channels. In this context, beam steering mechanisms can play a crucial role.

Compact and integrated beam splitters will be critical for controlling multi-mode plasmonic lasers' emission directions, augmenting the device's capability. Traditional beam splitters, such as prisms, coated plates, and gratings, are bulky and unsuitable for integrating into micro-optical circuits [3,4]. The advent of metamaterials and ultra-thin flat photonic structures such as metasurfaces has significantly mitigated this limitation. Metamaterials are synthetic composites featuring electromagnetic microstructures on deep-subwavelength scales. One can tailor arbitrary permittivity (ϵ) and permeability (μ) values with metamaterials, dramatically expanding the potential for light manipulation. Metamaterials, in conjunction with plasmonics, can combine the advantages of photonics and electronics by linking the energy and momentum of photons to a free electron gas through surface plasmons. On the other hand, metasurfaces are ultra-thin, flat photonic structures that can alter the polarization, phase, and amplitude of light in both reflection and transmission modes. Metasurfaces are notable for their high diffraction efficiency across various angles of incidence [29]. These innovations have allowed more flexible control in applications like spectral splitting and arbitrary beam steering. Further advances in the field have given rise to innovative methodologies. For instance, Wu et al. used anomalous dispersion of planar photonic crystals (PhCs) near the dielectric band edge to control the wavelength-dependent propagation of light [30]. Similarly, Sautter et al. utilized a temperature-dependent refractive-index shift in a nematic liquid crystal to dynamically tune electric and magnetic resonances in all-dielectric silicon nanodisk metasurfaces [31].

Recently, dielectric metasurfaces, possessing either a phase-gradient [32] or geometric phase variation [33], have been employed in various designs to construct highly efficient beam splitters. Despite requiring further optimization to overcome transmission losses, Zeng et al. demonstrated steerable beams in the far-field region using an optical phased array [34]. Nonetheless, the search for multi-channel and multi-functional applications of metasurfaces persists. Current beam splitters are often limited by their narrow operational bandwidth, preventing them from meeting the requirements of future photonic systems for multi-channel and multi-functional applications. To address this, Wang et al. proposed a novel design method of phase profile based on dielectric metasurfaces, displaying not only superior splitting efficiency but also multi-channel splitting capability [35]. Their flat multi-channel design involves phase gradients oriented in multiple directions and utilizes a low-loss titanium dioxide (TiO_2) nanocylinder as the metasurface. This

approach has shown promise in expanding beam splitters' operational range and functionality, thereby meeting the evolving needs of photonic systems.

The working principle of metasurfaces, akin to that of phased arrays for microwave radiation, is unparalleled in manipulating the wavefront of incident radiation, allowing for a diverse set of applications with sub-micrometer-scale features, including interferometry and spectroscopy [35]. Each antenna component gradually changes the phase response, accumulating over the entire metasurface unit cell to bend the incident light beam. In optical communication, bending and manipulating the path of light with metasurfaces for multi-channel communication is crucial [34,36]. The optical analog of radar technology, light detection and ranging (LiDAR) technology, also needs beam steering over a range of angles [37–39]. In addition, the fine control of metasurface-based beam steering can direct light onto densely arranged trapped ions for quantum computing [31,40–43].

In this work, we demonstrate the steering of each of the two spectral modes of a dual-mode PNL at distinct angles by integrating a phase-gradient metasurface on top of the laser. We analyze the phase-gradient metasurface's spatial radiation pattern and its dependence on incident beam wavelength. We observe the wavelength-dependent splitting of the emitted laser beam in the radiation pattern emerging from the PNL fitted with the metasurface. We also highlight the steering of the lasing beam by changing its emission angle through variations of some of the structural parameters of the metasurface.

2. Device characterization and simulation methodology

To achieve the beam steering capability in a nanolaser, we have modified the PNL structure presented in Ref. [27] by incorporating a phase-gradient metasurface analogous to those detailed in Ref. [35]. Figure 1 provides a schematic representation of the phase-gradient metasurface integrated into the PNL. The PNL in this work consists of an IR-140 dye-doped polyurethane (PU) layer as the active medium, sandwiched between a perforated gold (Au) layer and a distributed Bragg reflector (DBR), as shown in Figs. 2(a,b). The DBR consists of five alternating layers of TiO_2 and magnesium difluoride (MgF_2) followed by a final TiO_2 layer adjacent to the gain medium. Single-wavelength lasing in this class of devices was first reported in Ref. [44], while subsequent analysis by Azad et al. identified SPP modes as the primary drivers of the lasing action [21].

However, modifications to the nanohole arrangement, as outlined in Ref. [27], from a straightforward square nanohole array (NHA) to a merged configuration of two NHAs, enable the device to lase dual wavelengths. The merged lattice NHA is depicted in Fig. 2(a-right). Figure 2(b) shows the device configuration of the PNL that is modified in our quest for steering the two modes at two distinct angles. In this device, among the various structural parameters, the thickness of the terminal layer of the DBR is especially critical in modulating key lasing characteristics, such as wavelength, linewidth, and mode separation. For the focus of our analysis, we choose the device's structural parameters and gain medium, as presented in Fig. 1(a), effectively tuning the device for lasing wavelengths of 869 nm and 879 nm.

2.1. Design of gradient metasurface-based beam-splitter

The steering of the PNL's two lasing modes is facilitated by an integrated phase-gradient metasurface depicted in Figs. 2(c,d). This metasurface—the multi-channel beam-splitter—comprises TiO_2 nanocylinders with varying radii and a refractive index of 2.23. TiO_2 has low dispersion, a small thermal expansion coefficient, and a broad transparency window. It also has a comparatively higher refractive index among transparent metal oxides, making it suitable for metasurfaces as the appropriate high-index material. Additionally, unlike plasmonic metasurfaces, a TiO_2 based metasurface can avoid the ohmic loss associated with metals. These nanocylinders are placed onto a fused quartz substrate. The metasurface splits any beam incident from the substrate

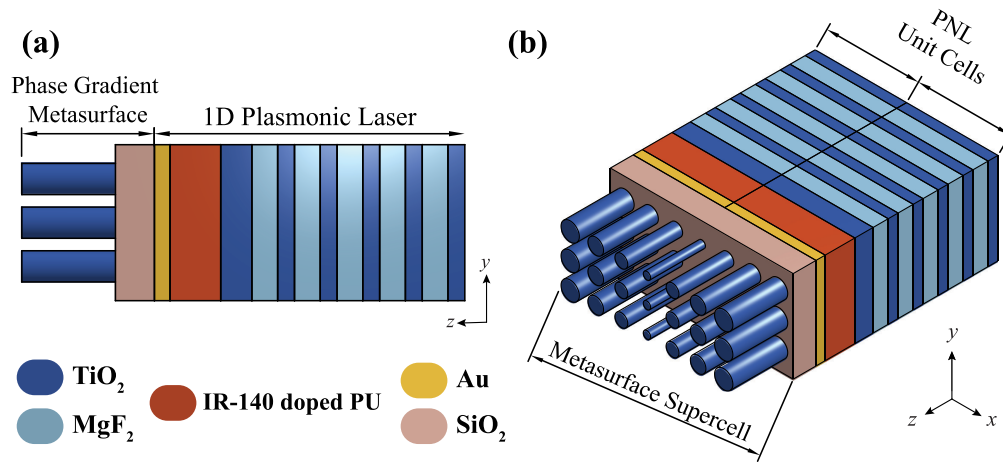


Fig. 1. Schematic illustration of the plasmonic nanolaser (PNL) integrated with a phase-gradient metasurface for beam splitting. (a) Side view of the combined device, comprising the metasurface and the 1D PNL. (b) Isometric view of the complete assembly: A single metasurface supercell aligns with two periods of the PNL along the x -axis and one period along the y -axis.

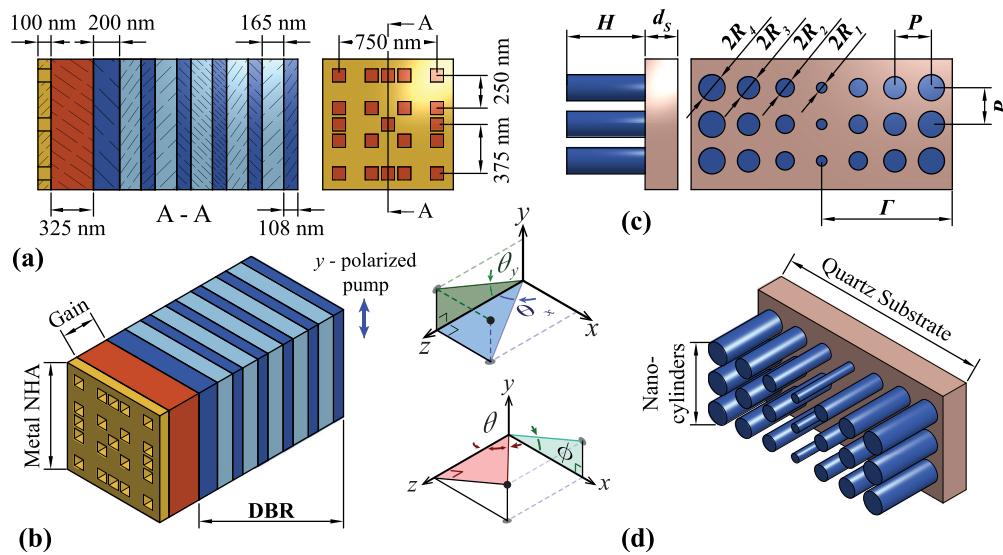


Fig. 2. Schematic illustration of the plasmonic nanolaser (PNL) and the phase-gradient metasurface. (a) Section view (left) along the A-A line on the front view (right) of the PNL. (b) Isometric view of the PNL, highlighting its constituent components. (c) Side (left) and front (right) views of the phase-gradient metasurface, consisting of TiO_2 nanocylinders on a SiO_2 substrate. The cylinder height is $H = 600$ nm, and inter-cylinder spacing is $P = 280$ nm. $\Gamma = 1240$ nm is the representation of a supercell's length in the gradient phase distribution. The radii of the nanocylinders increase gradually from the center towards the periphery of the metasurface - from R_1 to R_4 . (d) Isometric view of the metasurface.

side. The nanocylinders are arranged in rows in the x -direction, with each row consisting of seven cylinders that form a supercell. The cylinder with the smallest radius, R_1 , is located at the center of each supercell, and the radii of the cylinders increase gradually toward the periphery, culminating in the largest radius, R_4 , at the edge of the supercell. This design establishes a phase difference of $\pm\pi/2$ between adjacent nanocylinders, thereby creating at least two distinct phase gradient directions along the interface. The metasurface is designed to split an incident beam based on its wavelength, with the transmitted light diverging along the paths dictated by the phase gradient of the metasurface determined by the variation of the cylinder radii.

Consequently, multiple diffracted beams are expected to emerge in varying directions. By changing the size of the building blocks, it is possible to significantly vary the effective optical path length and, in turn, the transmitted wave's phase delay, thanks to TiO_2 's optical transparency and relatively large refractive index. The height of TiO_2 nanocylinders, H , is 600 nm, and the unit cell's period, P , is 280 nm. Figures 2(c,d) illustrate the selection of four distinct nanocylinders with radii of $R_1 = 40$ nm, $R_2 = 70$ nm, $R_3 = 85$ nm, and $R_4 = 100$ nm in order to maintain 2π phase coverage. The necessary structural and design parameters of the metasurface are presented in Table 1. When the normal incident plane wave transmits through the metasurface, a symmetric phase gradient is created in the x -direction, resulting in two transmission beams in the xy plane. We choose periodic boundary conditions in the x - and y -directions. In all the ensuing results, the propagation direction of an incident Gaussian wave with right-circular polarization is taken along $+z$ -direction.

Table 1. Designed beam splitter parameter values [35].

Parameters	Value
Substrate of the building block	SiO_2 (Glass) - Palik
Thickness of the Substrate, d_s	250 nm
Refractive index of TiO_2 nanocylinder	2.43
Height of the nanocylinder, H	600 nm
Period of the unit cell, P	280 nm
Radii of the nanocylinders	40, 70, 85, 100 nm
Length of supercell of gradient phase, Γ	1240 nm

To properly visualize beam steering in the far field, standard angles used in the spherical coordinate system, θ and ϕ , have been used to showcase the angular far-field intensity distribution, as shown in Fig. 2. The angle θ represents the polar angle formed by points in the far field with the z -axis. On the other hand, ϕ denotes the azimuth angle formed by the x -axis and the projection of the far-field point onto the transverse xy -plane. Aside from these standard notations, θ_x and θ_y demonstrated in Fig. 2 are the angles made by the points in the far-field plane with the yz and xz planes, respectively. In terms of spherical coordinates, $\theta = \theta_x$ when $\phi \in \{0^\circ, 180^\circ\}$ and $\theta = \theta_y$ when $\phi \in \{\pm 90^\circ\}$.

2.2. Simulation and numerical analysis methodology

To ascertain the electromagnetic dynamics governing the lasing activity, we employed the finite-difference time-domain (FDTD) method to solve three-dimensional full-field vectorial Maxwell's equations coupled with rate equations. This approach enabled us to obtain the requisite data for the PNL, the beam-splitter, and their integrated assembly in both time and frequency domains. Assessments were made on the lasing performance of the devices in near and far fields. Given the intrinsic periodicity of the PNL and beam-splitter in the x - and y -directions, we modeled a unit cell in these directions to enhance computational efficiency. Perfectly matched layer (PML) boundary conditions were applied in the z -direction in which the wave propagates.

The entire simulation space was discretized using a non-uniform conformal meshing method with a minimum mesh size of 0.25 nm. Convergence tests were performed to validate the mesh size and other simulation parameters.

Before integrating the beam-splitter metasurface with the laser, stand-alone simulations of the metasurface were conducted. A Gaussian pump source with an electric field amplitude of 1.8×10^8 V/m was utilized, emitting a plane wave pulse at an 850 nm wavelength with a 4 ps pulse duration and an 80 ps offset. This beam was injected perpendicular to the metasurface in the z -direction. To expedite the simulation, symmetric and anti-symmetric boundary conditions were applied in the x - and y -directions, capitalizing on the structure's inherent symmetry. Subsequent simulations of the integrated structure were performed in a similar environment using an FDTD method. An 800 nm Gaussian wave pulse with a 40 fs pulse length was the optical pump for these simulations.

A crucial aspect of accurately capturing the lasing dynamics of the PNL in FDTD simulations is the proper modeling of the gain medium's non-linear behavior. We adopted a semi-quantum mechanical approach based on a four-level, two-electron system, as detailed in Ref. [27]. This model incorporates quantized electron energies that have been simplified, resulting in four distinct energy levels for each of the two electrons [46,47]. In addition, this model contains Pauli's exclusion principle and the coupled rate equations of a four-level system [48]. This system is investigated using quantum mechanics, while the optical field is analyzed using classical mechanics [49].

All available charge carriers are initially located at the ground state, i.e., level 0. The incident pump pulse elevates these carriers to the highest energy level, corresponding to an absorption wavelength of 800 nm, followed by a non-radiative decay transition from the highest energy level, i.e., level 3 to 2. Radiative transitions predominantly contribute to the decay from level 2 to 1, corresponding to lasing emission at a wavelength of 870 nm. The emission and absorption wavelengths are not precisely aligned with the energy differences between the levels, resulting in finite linewidths for both processes. In addition, the decay lifetimes for non-radiative transitions are substantially shorter than those for radiative transitions. The specific parameters of the four-level, two-electron system for IR-140 dye molecules in a PU host matrix are listed in Table 2.

Table 2. Parameter values of the four-level two-electron gain medium model [45].

Parameter	Value
Emission wavelength, λ_a	870 nm
Emission linewidth, $\Delta\lambda_a$	100 nm
Absorption wavelength, λ_b	800 nm
Absorption linewidth, $\Delta\lambda_b$	100 nm
Gain medium base material index	1.51
Dye concentration	$2 \times 10^{18} \text{ cm}^{-3}$
Polarization decay rate, $\gamma_a = \gamma_b$	$3.9 \times 10^{13} \text{ s}^{-1}$
Radiative decay rate, γ_{rad}	$7.2 \times 10^7 \text{ s}^{-1}$
Transition lifetimes:	
$\tau_{30} = \tau_{21}$	1 ns
$\tau_{32} = \tau_{10}$	10 fs

2.3. Proposed experimental validation methodology

The proposed device can be fabricated on a glass substrate, with the TiO_2 - MgF_2 dielectric layers deposited using a high vacuum ion-assisted deposition technique. After that, the polymer layer

of polyurethane, mixed with IR-140 dye molecules, can be spin-coated, followed by thermal curing [47,50,51]. The gold film can be deposited using a thermal evaporation technique, and the holes can be etched onto the film through optimally controlled focused ion beam milling (FIB) or by template stripping on a suitable substrate [26,51–53]. While the FIB technique is adequate, template stripping is the method of choice for better resolution and smoother metal patterning.

While the broadband and passive response of the standalone gradient metasurface has been explored in earlier works, our work reports on using the metasurface monolithically integrated with an active laser. Thus, the ease of combining the metasurface with the planar face of the PNL is a rather welcome advantage for this design. The beam splitter-integrated sample laser can be tested by illuminating it using a Ti:sapphire pulsed laser, emitting a 40 fs pulse at 800 nm with a 1 kHz repetition rate. After passing through a polarizer, the pump beam can be collimated onto the device with an elliptical spot roughly the same size as the dimensions of the PNL. After that, the emitted laser beam can be observed with a charge-coupled device (CCD) camera at the select emission angles. The beams can be collected at different angles and analyzed with a spectrometer to identify the wavelengths of the respective beams. The spectrum of each deviated beam can be used to confirm the wavelength-selective nature of beam steering [25,47,54].

3. Results and discussion

3.1. Lasing emission: near-field and far-field modes

The dual optical resonance in the proposed PNL is principally caused by the merged lattice NHA on an Au thin film [27,55]. The excitation of surface plasmons at the metal-gain medium interface and LSPs at the metal nanoholes creates the resonant modes [56]. These plasmonic modes emerge as radiative modes through the sub-wavelength nanoholes as extraordinary optical transmission (EOT), boosting the transmission across the metal NHA and generating a series of peaks and valleys in the near- and far-field transmission profiles [57]. The transmission coefficient (T) through a single sub-wavelength hole is given by Bethe [57] and Bouwkamp [58] as $T \approx 64r^4 / (27\pi^2 \lambda_0^4)$, where r is the hole radius, and λ_0 is the incident wavelength. The periodic configuration of holes on the metal film further enhances this transmission in addition to acting like a plasmonic resonator.

Figure 3(a) illustrates the lasing emission spectrum of the merged lattice PNL depicted in Figs. 2(a,b), where the gain medium is doped with IR-140 dye molecules. The lasing emission occurs at two distinct modes at 869 and 879 nm. The resonance is due to the coexistence of two different surface plasmon modes at the nanoholes. The sub-wavelength periodicity of the merged lattice metal nanoholes enables the suggested structure to generate only the zeroth-order mode. This overcomes the inherent drawback of conventional plasmonic lasers, which emit higher-order spatial modes due to the mismatch between the wave vectors of free-space propagating waves and those of SPP modes. The merged lattice metal NHA's two-fold periodicity has contributed to the convergence of spatial modes in the far field [59].

The far-field intensity profile was calculated by uniformly illuminating the PNL in Figs. 2(a,b) and projecting the near-field intensity onto a hemispherical surface 1 meter from the PNL. As our PNL is a periodic structure, the number of lattice periods of the structure along the transverse directions impacts the far-field pattern. Therefore, the PNL is assumed to have a transverse area of $150 \mu\text{m} \times 150 \mu\text{m}$. Figure 3(b) shows the angular intensity distribution for $\phi \in \{0^\circ, 90^\circ\}$ obtained from the full two-dimensional (2D) far-field projection of the PNL, where θ denotes the angles formed by the points of the far-field plane with the z -axis. The obtained far-field distribution profiles were normalized to the intensity of the pump pulse. The periodicity of the lattice and the two-fold symmetry in the periodic merged arrangement result in significantly greater constructive interference in the far field, creating a small divergence angle of $<0.35^\circ$ in the far field.

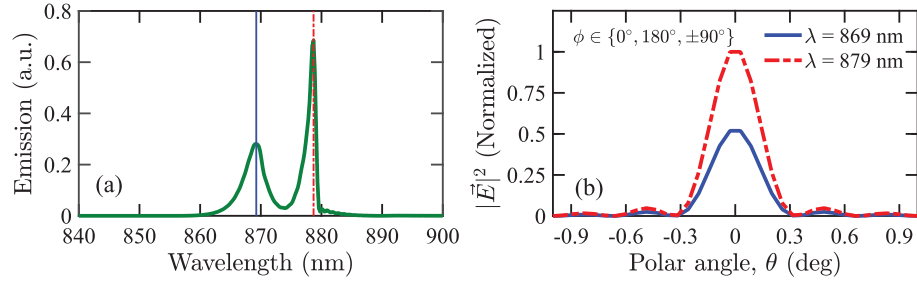


Fig. 3. (a) The near-field laser emission spectrum of the standalone PNL structure in Figs. 2(a,b) shows two distinct modes. (b) The angular distribution of far-field intensity of both the lasing modes in (a), for select azimuthal angles, ϕ .

3.2. Response of the beam-splitter

Gradient metasurfaces can control light by imparting local phase alterations to the incident electromagnetic waves [60–62]. Such metasurfaces are devised to exhibit spatially varying optical responses, resulting in scattered fields with spatially variable amplitudes, phases, and polarizations [62]. The phase response of the incident beam through the metasurface can be described by the generalized Snell's laws

$$k_x^{(r)} - k_x^{(i)} = \frac{d\Phi}{dx}, \quad (1a)$$

$$k_x^{(t)} - k_x^{(i)} = \frac{d\Phi}{dx}, \quad (1b)$$

$$k_x^{(i,r,t)} = k_0 n_{(i,r,t)} \sin \theta_{(i,r,t)}. \quad (1c)$$

The generalized Snell's law represents the relationship between the incident plane wave with the refracted or reflected light wave where θ_i is the angle between the incident plane wave and the surface normal of the metasurface, k_0 is the free-space wave number, $\Phi = \Phi(x)$ is the position-dependent phase profile of the incident wave through the metasurface, and $k_x^{(i,r,t)}$ is the in-plane wave vector component. The superscripts (i) , (r) and (t) represent the incident, reflected and transmitted components of the radiation respectively.

It is evident that when $d\Phi/dx = 0$, the usual laws of reflection and refraction are conserved, implying the continuity of the in-plane wave vector. In contrast, a non-zero phase gradient, i.e., $d\Phi/dx \neq 0$, through a metasurface enables the decoupling of the angles of incidence and reflection or refraction, leading to anomalous optical behaviors. The most illustrative example of this anomalous behavior is featuring the metasurface as a linearly varying phase of the form $\Phi = \pm 2\pi x/\Lambda$, where Λ is the distance at which the phase shifts by 2π , thus imposing an additional in-plane wave number of $d\Phi/dx = \pm 2\pi/\Lambda$ on the reflected and refracted light.

Since plasmonic metasurfaces exhibit significant metal loss [63], dielectric metasurfaces of a high dielectric constant material are proposed, demonstrating high efficiency in adjusting beam deflection and polarization in transmission or reflection modes. Usually, the incident beam is divided at the metasurface, splitting the transmitted light. The transmitted beams are expected to refract in multiple directions along the direction of each phase gradient. The angle of a split beam can be determined using the generalized Snell's law: $n_t \sin \theta_t - n_i \sin \theta_i = (\lambda_0/2\pi)d\Phi/dr$ [35], where n_i and n_t denote the refractive indices of the incident and the refraction medium, respectively, θ_i and θ_t denote the incident and the refraction angles, λ_0 denotes the wavelength of light at vacuum, and $d\Phi/dr$ denotes the phase gradient imparted along the metasurface. The results of the far-field radiation intensity distribution of the 850 nm mode transmitted through

the beam-splitter are presented in Fig. 4, where the maximum intensity of the field indicates the direction of the emitted beams. It is observed that for azimuth angles of $\phi = \pm 90^\circ$ the emitted beam is split in two directions with a polar deflection angle of $\theta = 27^\circ$, i.e., $\theta_y = \pm 27^\circ$. However, along $\phi = 180^\circ$, only a single radiation lobe remains undeviated.

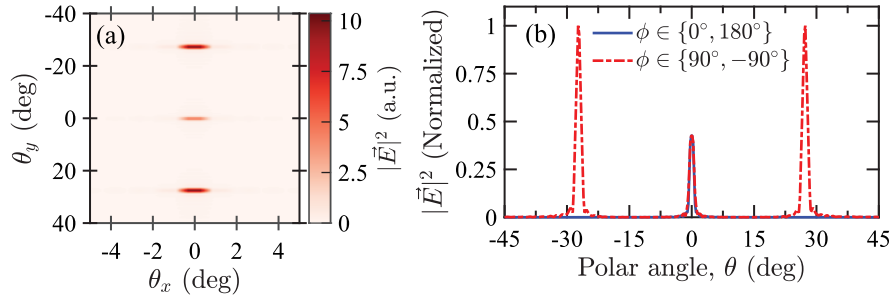


Fig. 4. (a) Angular distribution of the far-field radiation intensity profile and (b) the far-field intensity distribution normalized to the peak intensity at selected values of ϕ for the beam-splitter. The beam-splitter is pumped by a y-polarized 850 nm wavelength source.

To investigate the effects of the incident beam's wavelength on beam steering, three different pump sources of wavelength 800, 850, and 880 nm have been applied separately to the splitter, and the results are shown in Fig. 5. The response for $\lambda = 800$ nm has only one peak intensity, i.e., the beam is not split and goes along the same direction as the incident beam, as shown in Figs. 5(a,b). For $\lambda = 850$ nm, the transmitted beam is split into two beams with a deflection angle of $\theta = 27^\circ$ and $\phi = \pm 90$, similar to the results in Fig. 4. The central lobe in Fig. 5(d) is due to the directly transmitted wave and is relatively small compared to the two deflected beams. The transmitted beam for $\lambda = 880$ nm, on the other hand, is split into four notable beams along a deflection angle of $\theta = 37^\circ$ having a transverse angular distribution along four channels dictated by $\phi = \pm 51^\circ \pm 180^\circ$, respectively, as shown in Figs. 5(e, f). However, in this case, the peak beam intensity is further lessened to eleven times the maximum intensity for $\lambda = 880$ nm. Furthermore, at 880 nm, the beam-splitter can also emit more deflected beams along $\theta = 22^\circ$ and $\theta = 27^\circ$, but at an even lower intensity oriented along $\phi \in \{0^\circ, 180^\circ\}$ and $\phi \in \{\pm 90^\circ\}$, respectively. The electric field intensity profile of the transmitted beams is shown in Fig. 5(e). The emission at $\lambda = 800$ nm has the highest intensity.

3.3. Response of the integrated structure

Figure 6(a) shows the emission spectra of the overall structure, indicating that the emission occurs mainly via two dominant modes at 870 nm and 883 nm. These resonances can be attributed to the two distinct surface plasmon modes localized at the nanoholes. Additionally, there are two subordinate modes near 860 nm and 900 nm. However, their transmission amplitudes are quite low compared to the dominant modes, allowing them to be ignored for the analysis of the emitted beam without significant loss in accuracy. It is also notable that merging both structures slightly alters the intensity of the peak wavelengths and the overall response of the stand-alone dual-mode laser.

The far-field intensity distribution of the two modes is shown in Fig. 6(b), illustrating the spatially intact mode at 870 nm and the split mode at 883 nm. The intensity distribution of the 870 nm beam shows slower decay of intensity along the axis of excitation, i.e., y-axis, than along the non-exciting axis. However, no lobe of the intensity distribution is distinct enough to be considered as splitting of the beam. The emitted beam at 883 nm has a central lobe and two more split beams of similar intensity with an angular deviation of 23° from the central lobe. Two more beams, albeit of lower intensity, are also seen to emerge, having split at an angle of $\theta \approx 50^\circ$

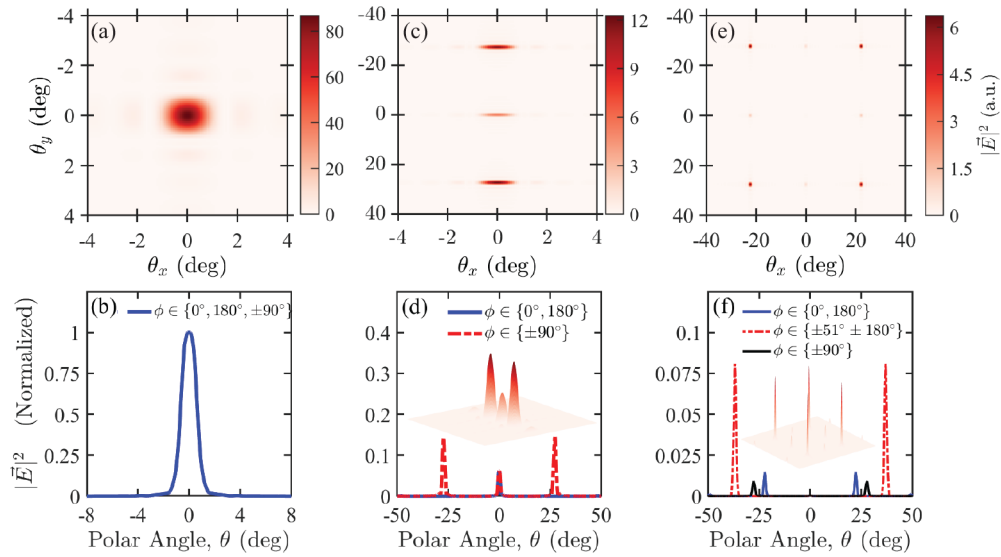


Fig. 5. Angular distribution of the far-field radiation intensity profile (a,c,e) and far-field intensity distribution normalized to the peak far-field intensity at $\lambda = 800$ nm for some selected values of ϕ (b,d,f) for the beam-splitter. The excitation wavelengths for the above results are as follows: (a,b) $\lambda = 800$ nm, (c,d) $\lambda = 850$ nm and (e,f) $\lambda = 880$ nm.

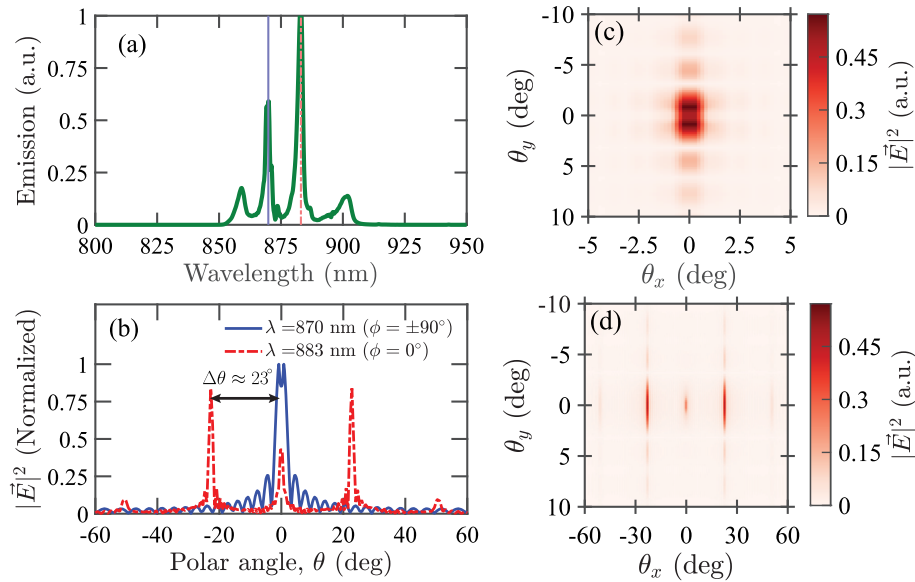


Fig. 6. (a) Lasing emission spectrum of the PNL integrated with the beam-splitter. (b) Far-field intensity distribution normalized to the peak intensity at selected values of ϕ for the two dominant emission modes of the integrated laser at 870 nm and 883 nm. Angular distribution of the far-field radiation intensity profile at (c) $\lambda = 870$ nm and (d) $\lambda = 883$ nm.

from the center. Therefore, we get split beams from the two principal modes where the angular separations between the beams of the two modes are almost 23° and 50° , respectively. However, the second radiation lobe of the 883 nm mode at $\theta = 50^\circ$ is negligible compared to the maximum intensity at that wavelength. Thus, we essentially get two beams from the two principal modes, having an angular separation of 23° instead of three. Figures 6(c,d) illustrate the electric field profile of the two discussed lasing modes.

3.3.1. Effect of the radius of nanocylinders

Increasing or decreasing the radii of the constituent nanocylinders of the beam-splitter changes the far-field intensity distribution of the device. The far-field radiation lobes show greater angular separation when the nanocylinder radii are smaller than those listed in Table 1. Conversely, for larger radii, the pattern becomes more converged, although becoming more diffusive and lacking distinct, well-isolated lobes. The intensity distribution of the two lasing modes at 865 nm and 875 nm, along $\phi = 0^\circ$ is shown in Fig. 7. For the case in Fig. 7(a), when the nanocylinder radii are reduced by 20 nm so that they are 20, 50, 65, and 80 nm, we note two significant beam splittings: One for 865 nm at $\theta = 0^\circ$ and one for 875 nm at a deflection angle of $\theta \approx 62^\circ$. The angular separation between the two modes increases from the $\sim 23^\circ$ observed in the intensity profile of Fig. 6(b) to $\sim 62^\circ$ in Fig. 7.

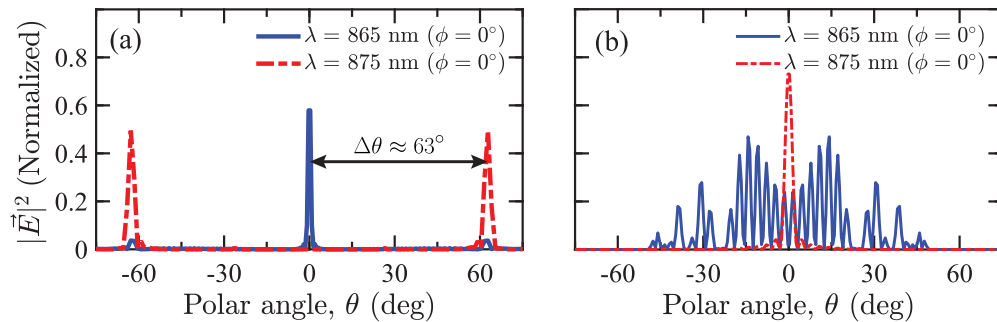


Fig. 7. Far-field intensity distribution, normalized to peak intensity, for the two dominant emission modes (at λ) of the integrated laser. This is shown at select values of ϕ for varying radii of nanocylinders in the beam-splitter metasurface. The far-field profiles for nanocylinder radii of (a) 20, 50, 65, and 80 nm, and (b) 60, 90, 105, and 120 nm are shown.

Figure 7(b) depicts the response of increasing all the nanocylinder radii by 20 nm; i.e., nanocylinder radii are 60, 90, 105, and 120 nm. For $\phi = 0^\circ$, the angular distribution of the 875 nm mode remains unchanged from that in Fig. 7(a). However, for the same ϕ , the 865 nm mode does not have any distinct emission lobe but rather multiple closely spaced lobes, indicative of the absence of effective beam-steering or splitting. The envelope of the 865 nm mode profile peaks at $\theta \approx 14^\circ$, exhibiting a smaller beam separation than that in Fig. 6(b) and Fig. 7(a) and suggesting that the magnitudes of the nanocylinders' radii are inversely related to the angular separation of the modes. This effect arises because light traversing through the metasurface encounters a mixed medium of TiO_2 and air. Therefore, an alteration in the lateral geometry of the metasurface, by changing the nanocylinder radii, modifies the effective refractive index of the medium. Consequently, this variation increases the phase difference between adjacent unit cells according to the relationship $\Phi = (2\pi/\lambda)n_{\text{eff}}$, where Φ represents the phase change, n_{eff} the effective refractive index, and λ the wavelength of the incident light.

3.3.2. Effect of number of supercell rows

In preceding simulations, we have used 3 rows of identical supercells, as shown in Fig. 2(b). Figure 8 shows that the far-field intensity distribution results when we increase the number of supercell rows to 5. The electric field intensity profile of the two lasing modes is presented in Figs. 8(a,b). The lower wavelength mode, emitting at a different wavelength than in Fig. 6(c), emits at 869 nm, and contrary to the lack of splitting in Fig. 6(c), the emitted beams achieve splitting along the y -axis. The higher wavelength mode, on the other hand, is split spatially into four beams, each being approximately $\sim 90^\circ$ apart from each other along the ϕ axis.

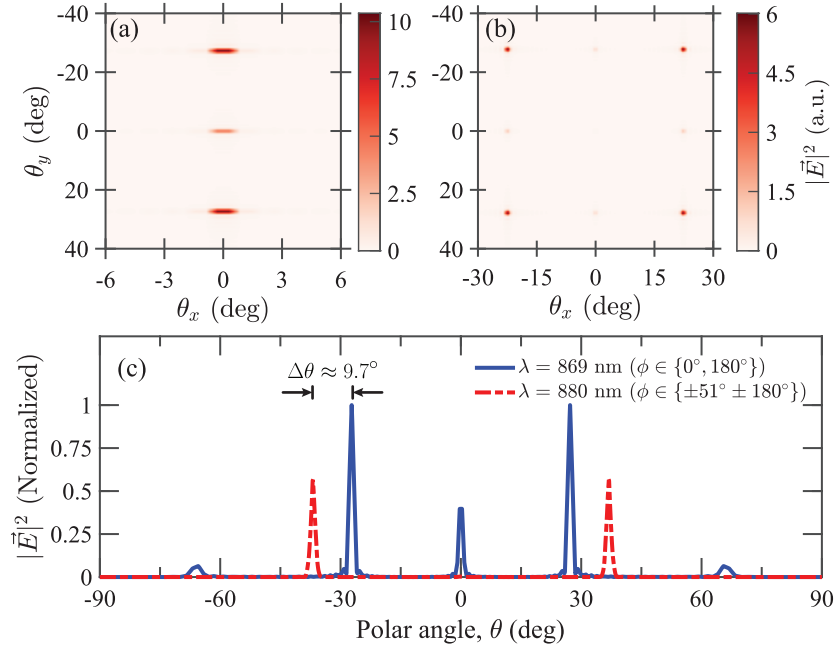


Fig. 8. Angular distribution of the far-field radiation intensity profile of the PNL integrated with beam-splitter having 5 supercell rows at (a) $\lambda = 869$ nm and (b) $\lambda = 880$ nm. (c) Far-field intensity distribution, normalized to peak intensity, for the two emission modes shown in (a,b) at select values of ϕ .

In contrast to the single un-deviated emission lobe at the lower wavelength mode in Fig. 6(b) for the metasurface having 3 supercell rows, three separate beams along $\theta = 0^\circ, \pm 27^\circ$ are observed for the lower wavelength mode in Fig. 8(c). The deviated lower mode beams have almost twice the intensity than that of the un-deviated lobe of the same mode at $\theta = 0^\circ$. At the higher wavelength mode of 880 nm, two distinct beams deflected along $\theta \approx 36.9^\circ$ are observed for $\phi \in \{\pm 51^\circ\}$. The angular separation between the highest peaks of the two modes is approximately $\sim 9.7^\circ$, implying a significant reduction in separation compared to Fig. 6. From Fig. 8(c), we note that the deflection between two split beams at 869 nm is $\theta \approx 27^\circ$ for $\phi \in \{0^\circ, 180^\circ\}$. Figures 8(b,c) show four split beams for 880 nm with $\theta \approx 40^\circ$, and their respective azimuth angles are $\phi \in \{\pm 45^\circ \pm 180^\circ\}$. The peak intensity of 869 nm is noted to be greater than that of 880 nm. The spatial separation between the modes has decreased from that in Fig. 6, but the intensity of the smaller wavelength mode for the case of 5 supercell rows is greater than that observed for 3 supercell rows. Therefore, increasing the number of supercell rows increases the splitting of beams but reduces the angular separation between the lobes of different modes. As the number of splitting beams increases, the electric field intensity of each splitting beam decreases.

3.3.3. Practical considerations

Our reported laser can diverge beams up to $\sim 63^\circ$. The emission angles and number of steered beams can be tuned by changing the nanocylinder radius and the number of nanocylinder rows. The steering range of our laser is comparable to that reported recently in literature [31,32,34]. However, unlike the dynamic beam steering in some of these applications, this structure is fixed for an instance of fabrication. The capability of dynamic tuning may be incorporated by having a material whose index can be controlled by external voltage or temperature. Recently, Ref. [64] showed beam divergence only between two steering states.

We reference the findings discussed earlier in this section to assess the impact of fabrication defects on device performance and beam-steering sensitivity. It is observed that an increase in the radii of nanocylinders introduces a threshold radius beyond which the emission becomes diffused and loses directionality. However, for radii up to 20 nm smaller than the standard values mentioned in Table 1, there will be no loss of directionality. Thus, we can conclude that the nanocylinder radii have a tolerance threshold of at least 20 nm from the values listed in Table 1, within which the emission directionality and beam steering properties will be preserved.

The device presented in this work can be incorporated into a larger integrated photonic system with additional steps. In recent years, three-dimensional (3D) nanofabrication techniques such as laser-induced transfer (LIT), light-directed assembly, and inkjet printing have been utilized to manufacture similar devices on a silicon-nitride or any other suitable photonic platform [32,65]. Furthermore, the metasurface can even be fabricated through additive manufacturing on top of the plasmonic laser after integrating onto a photonic platform [66]. Thanks to the inherent periodicity of the device, we can scale the device as part of a larger system, as per our requirement. However, to create a fully-fledged photonic system with our device as one of the components, we would also need to optimize the in and out-coupling of radiation in the system. This process would require further optimization of the interface components, which is beyond the scope of this work.

4. Conclusion

We have demonstrated an integrated dual-mode PNL capable of steering lasing emission differentially with wavelength. The demonstrated device not only exhibits steering of the emitted beam but also enables wavelength-dependent control over steering. The wavelength-specific steering is enabled by integrating a phase-gradient metasurface, which functions as a beam-splitter, with the PNL. This integration allows for distinct steering of the dual-mode laser's two emissions. The wavelength-selective steering response of the metasurface is confirmed through numerical simulations, guiding the design of a customized metasurface to direct beams at specific wavelengths emitted from the PNL. The lasing emission characteristics of the integrated steerable PNL have been presented, and distinctive angular separation for different wavelengths has been shown. The far-field response of the system for variation of metasurface parameters showcases the customizability of the device and the possibility to tailor emission along arbitrary angles. Our work demonstrates the potential of spatially separating lasing emission from plasmonic lasers, opening up new degrees of freedom for our PNL lasing emission. This device represents an advancement towards the realization of a fully customizable and dynamically tunable plasmonic laser capable of on-demand emission control in terms of both angles and wavelengths. The proposed device can be integrated with suitable photonic platforms, with additional optimizations for proper functioning.

Disclosures. The authors declare that they have no conflict of interest.

Data availability. Data underlying the results presented in this paper are not publicly available at this time but may be obtained from the authors upon reasonable request.

References

1. A. S. Pradeep, G. A. Bidkar, D. Thippesha, *et al.*, "Design of Compact Beam-Steering Antenna with a Novel Metasubstrate Structure," in *2020 IEEE International Conference on Distributed Computing, VLSI, Electrical Circuits and Robotics*, (2020), pp. 96–99.
2. T. K. Chan, M. Megens, and B.-W. Yoo, "Optical beamsteering using an 8×8 MEMS phased array with closed-loop interferometric phase control," *Opt. Express* **21**(3), 2807–2815 (2013).
3. B. Wang, C. Zhou, and J. Feng, "Wideband two-port beam splitter of a binary fused-silica phase grating," *Appl. Opt.* **47**(22), 4004–4008 (2008).
4. C. Xiang, C. Xiang, and C. Zhou, "Five-port beam splitter of a single-groove grating," *Chin. Opt. Lett.* **16**(7), 070501 (2018).
5. Y.-J. Lin, K.-M. Chen, and S.-T. Wu, "Broadband and polarization-independent beam steering using dielectrophoresis-tilted prism," *Opt. Express* **17**(10), 8651–8656 (2009).
6. V. V. Mai and H. Kim, "Non-mechanical beam steering and adaptive beam control using variable focus lenses for free-space optical communications," *J. Lightwave Technol.* **39**(24), 7600–7608 (2021).
7. M. Duval, G. Fortin, M. Piché, *et al.*, "Tuning of external-cavity semiconductor lasers with chirped diffraction gratings," *Appl. Opt.* **44**(24), 5112–5119 (2005).
8. P. Zorabedian, "Characteristics of a grating-external-cavity semiconductor laser containing intracavity prism beam expanders," *J. Lightwave Technol.* **10**(3), 330–335 (1992).
9. C. J. Hawthorn, K. P. Weber, and R. E. Scholten, "Littrow configuration tunable external cavity diode laser with fixed direction output beam," *Rev. Sci. Instrum.* **72**(12), 4477–4479 (2001).
10. R. F. Oulton, V. J. Sorger, and T. Zentgraf, "Plasmon lasers at deep subwavelength scale," *Nature* **461**(7264), 629–632 (2009).
11. L. Novotny and S. J. Stranick, "Near-field optical microscopy and spectroscopy with pointed probes," *Annu. Rev. Phys. Chem.* **57**(1), 303–331 (2006).
12. T. W. Johnson, Z. J. Lapin, and R. Beams, "Highly reproducible near-field optical imaging with sub-20-nm resolution based on template-stripped gold pyramids," *ACS Nano* **6**(10), 9168–9174 (2012).
13. M. I. Stockman, "Nanoplasmonic sensing and detection," *Science* **348**(6232), 287–288 (2015).
14. R.-M. Ma and R. F. Oulton, "Applications of nanolasers," *Nat. Nanotechnol.* **14**(1), 12–22 (2019).
15. Z. Xie, W. Yu, and T. Wang, "Plasmonic nanolithography: a review," *Plasmonics* **6**(3), 565–580 (2011).
16. W. Srituravanich, N. Fang, and C. Sun, "Plasmonic nanolithography," *Nano Lett.* **4**(6), 1085–1088 (2004).
17. J. N. Anker, W. P. Hall, and O. Lyandres, "Biosensing with plasmonic nanosensors," *Nat. Mater.* **7**(6), 442–453 (2008).
18. J. Homola, "Surface Plasmon Resonance Sensors for Detection of Chemical and Biological Species," *Chem. Rev.* **108**(2), 462–493 (2008).
19. I. P. Radko, M. G. Nielsen, O. Albrektsen, *et al.*, "Stimulated emission of surface plasmon polaritons by lead-sulphide quantum dots at near infra-red wavelengths," *Opt. Express* **18**(18), 18633–18641 (2010).
20. M. T. Hill, Y.-S. Oei, and B. Smalbrugge, "Lasing in metallic-coated nanocavities," *Nat. Photonics* **1**(10), 589–594 (2007).
21. Z. Ahmed and M. A. Talukder, "An efficient and directional optical Tamm state assisted plasmonic nanolaser with broad tuning range," *J. Phys. Commun.* **2**(4), 045016 (2018).
22. Y. Huo, T. Jia, and T. Ning, "A low lasing threshold and widely tunable spaser based on two dark surface plasmons," *Sci. Rep.* **7**(1), 13590 (2017).
23. J.-S. Wu, V. Apalkov, and M. I. Stockman, "Topological spaser," *Phys. Rev. Lett.* **124**(1), 017701 (2020).
24. Z. Azad and M. A. Talukder, "Simultaneously surface- and edge-emitting plasmonic laser operating in the near-infrared region," *Opt. Laser Technol.* **146**, 107571 (2022).
25. S. Pourjamal, T. K. Hakala, and M. Nečada, "Lasing in Ni nanodisk arrays," *ACS Nano* **13**(5), 5686–5692 (2019).
26. J. M. Winkler, M. J. Ruckriegel, and H. Rojo, "Dual-Wavelength Lasing in Quantum-Dot Plasmonic Lattice Lasers," *ACS Nano* **14**(5), 5223–5232 (2020).
27. S. Shahid, S.-E. Zumrat, and M. A. Talukder, "A merged lattice metal nanohole array based dual-mode plasmonic laser with an ultra-low threshold," *Nanoscale Adv.* **4**(3), 801–813 (2022).
28. S. E. Zumrat, S. Shahid, and M. A. Talukder, "Dual-wavelength hybrid tamm plasmonic laser," *Opt. Express* **30**(14), 25234–25248 (2022).
29. M. W. Knight, H. Sobhani, P. Nordlander, *et al.*, "Photodetection with active optical antennas," *Science* **332**(6030), 702–704 (2011).
30. L. Wu, M. Mazilu, and T. Krauss, "Beam steering in planar-photonic crystals: from superprism to supercollimator," *J. Lightwave Technol.* **21**(2), 561–566 (2003).
31. J. Sautter, I. Staude, and M. Decker, "Active tuning of all-dielectric metasurfaces," *ACS Nano* **9**(4), 4308–4315 (2015).
32. Z. Li, M.-H. Kim, and C. Wang, "Controlling propagation and coupling of waveguide modes using phase-gradient metasurfaces," *Nat. Nanotechnol.* **12**(7), 675–683 (2017).
33. W. Luo, S. Sun, and H.-X. Xu, "Transmissive ultrathin Pancharatnam-Berry metasurfaces with nearly 100% efficiency," *Phys. Rev. Appl.* **7**(4), 044033 (2017).

34. Y.-S. Zeng, S.-W. Qu, B.-J. Chen, *et al.*, “All-plasmonic optical phased array integrated on a thin-film platform,” *Sci. Rep.* **7**(1), 9959 (2017).
35. J. Wang, Q. Jiang, and D. Han, “Multi-channel beam splitters based on gradient metasurfaces,” *Results Phys.* **24**, 104084 (2021).
36. D. M. Solís, J. M. Taboada, F. Obelleiro, *et al.*, “Optimization of an optical wireless nanolink using directive nanoantennas,” *Opt. Express* **21**(2), 2369–2377 (2013).
37. Z. Wang, W. Song, and Y. Chen, “Metasurface empowered lithium niobate optical phased array with an enlarged field of view,” *Photonics Res.* **10**(11), B23–B29 (2022).
38. W.-B. Lee, W.-B. Lee, and C.-S. Im, “Metasurface doublet-integrated bidirectional grating antenna enabling enhanced wavelength-tuned beam steering,” *Photonics Res.* **10**(1), 248–255 (2022).
39. J. Xu, M. Cua, and E. H. Zhou, “Wide-angular-range and high-resolution beam steering by a metasurface-coupled phased array,” *Opt. Lett.* **43**(21), 5255–5258 (2018).
40. M. Shirao, D. Klawson, S. Mouradian, *et al.*, “Integrated beam steering using a 2d focusing grating coupler for scalable trapped ion quantum computing,” in *2022 27th OptoElectronics and Communications Conference (OECC) and 2022 International Conference on Photonics in Switching and Computing (PSC)*, (2022), pp. 1–4.
41. R. C. Souza, W. F. Balthazar, and J. A. O. Huguenin, “Universal quantum gates for path photonic qubit,” *Quantum Inf. Process.* **21**(2), 68 (2022).
42. C. Knoernschild, C. Kim, and B. Liu, “MEMS-based optical beam steering system for quantum information processing in two-dimensional atomic systems,” *Opt. Lett.* **33**(3), 273–275 (2008).
43. K. Wang, M. Chekhova, and Y. Kivshar, “Metasurfaces for quantum technologies,” *Phys. Today* **75**(8), 38–44 (2022).
44. Z. Azad, Md. Shofiqul Islam, and M. A. Talukder, “Mode-resolved analysis of a planar multi-layer plasmonic nanolaser,” *Opt. Commun.* **482**, 126614 (2021).
45. S. A. Maier, *Plasmonics: Fundamentals and Applications* (Springer US, New York, NY, 2007).
46. M. Dridi and G. C. Schatz, “Model for describing plasmon-enhanced lasers that combines rate equations with finite-difference time-domain,” *J. Opt. Soc. Am. B* **30**(11), 2791–2797 (2013).
47. W. Zhou, M. Dridi, and J. Y. Suh, “Lasing action in strongly coupled plasmonic nanocavity arrays,” *Nat. Nanotechnol.* **8**(7), 506–511 (2013).
48. H. Yokoyama and S. D. Brorson, “Rate equation analysis of microcavity lasers,” *J. Appl. Phys.* **66**(10), 4801–4805 (1989).
49. C. H. Townes, *How the Laser Happened: Adventures of a Scientist* (Oxford University Press, New York Oxford, 1999).
50. A. Yang, T. B. Hoang, M. Dridi, *et al.*, “Real-time tunable lasing from plasmonic nanocavity arrays,” *Nat. Commun.* **6**(1), 6939 (2015).
51. P. N. Melentiev, A. E. Afanasiev, and A. A. Kuzin, “Single nanohole and photonic crystal: wavelength selective enhanced transmission of light,” *Opt. Express* **19**(23), 22743–22754 (2011).
52. D. Adams, M. Vasile, C. Hodges, *et al.*, “Focused ion beam fabrication of nanopores in metal and dielectric membranes,” *Microsc. Microanal.* **13**(S02), 1512–1513 (2007).
53. P. Nagpal, N. C. Lindquist, S.-H. Oh, *et al.*, “Ultrasoft patterned metals for plasmonics and metamaterials,” *Science* **325**(5940), 594–597 (2009).
54. F. Ding, Y. Chen, and S. I. Bozhevolnyi, “Gap-surface plasmon metasurfaces for linear-polarization conversion, focusing, and beam splitting,” *Photonics Res.* **8**(5), 707–714 (2020).
55. G. Alagappan and C. E. Png, “Localization of waves in merged lattices,” *Sci. Rep.* **6**(1), 31620 (2016).
56. A. Degiron and T. W. Ebbesen, “The role of localized surface plasmon modes in the enhanced transmission of periodic subwavelength apertures,” *J. Opt. A: Pure Appl. Opt.* **7**(2), S90–S96 (2005).
57. H. A. Bethe, “Theory of diffraction by small holes,” *Phys. Rev.* **66**(7-8), 163–182 (1944).
58. C. J. Bouwkamp, “Diffraction theory,” *Rep. Prog. Phys.* **17**(1), 35–100 (1954).
59. I. V. Treshin, V. V. Klimov, P. N. Melentiev, *et al.*, “Optical tamm state and extraordinary light transmission through a nanoaperture,” *Phys. Rev. A* **88**(2), 023832 (2013).
60. A. Boltasseva and H. A. Atwater, “Low-loss plasmonic metamaterials,” *Science* **331**(6015), 290–291 (2011).
61. D. Lin, P. Fan, E. Hasman, *et al.*, “Dielectric gradient metasurface optical elements,” *Science* **345**(6194), 298–302 (2014).
62. F. Ding, A. Pors, and S. I. Bozhevolnyi, “Gradient metasurfaces: a review of fundamentals and applications,” *Rep. Prog. Phys.* **81**(2), 026401 (2018).
63. L. Yang, D. Wu, and Y. Liu, “High-efficiency all-dielectric transmission metasurface for linearly polarized light in the visible region,” *Photonics Res.* **6**(6), 517–524 (2018).
64. M. Khodadadi, N. Nozhat, and S. M. M. Moshiri, “Theoretical analysis of a graphene quantum well hybrid plasmonic waveguide to design an inter/intra-chip nano-antenna,” *Carbon* **189**, 443–458 (2022).
65. J. E. Melzer and E. McLeod, “3D Nanophotonic device fabrication using discrete components,” *Nanophotonics* **9**(6), 1373–1390 (2020).
66. A. Yulaev, W. Zhu, and C. Zhang, “Metasurface-integrated photonic platform for versatile free-space beam projection with polarization control,” *ACS Photonics* **6**(11), 2902–2909 (2019).